



Coexistence of air and dielectric modes in single nanocavity

FUJUN SUN,^{1,2,3} JINGXUAN WEI,^{2,3} BOWEI DONG,^{2,3} YIMING MA,^{2,3} YUHUA CHANG,^{2,3} HUIPING TIAN,^{1,4} AND CHENGKUO LEE^{2,3,5}

¹State Key Laboratory of Information Photonics and Optical Communications, Beijing University of Posts and Telecommunications, Beijing 100876, China

²Department of Electrical and Computer Engineering, National University of Singapore, 117583, Singapore

³Center for Intelligent Sensors and MEMS, National University of Singapore, 117608, Singapore

⁴hptian@bupt.edu.cn

⁵elelc@nus.edu.sg

Abstract: A deterministic design method and experimental demonstration of single photonic crystal nanocavity supporting both air and dielectric modes in the mid-infrared wavelength region are reported here. The coexistence of both modes is realized by a proper design of photonic dispersion to confine air and dielectric bands simultaneously. By adding central mirrors to make the resonance modes be confined at the bandgap edges, high experimental Q -factors of 2.32×10^4 and 1.59×10^4 are achieved at the resonance wavelength of about $3.875\mu\text{m}$ and $3.728\mu\text{m}$ for fundamental dielectric and air modes, respectively. Moreover, multiple sets of air and dielectric modes can be realized by introducing central aperiodic mirrors with multiple bandgaps. The realization of coexistence of air and dielectric modes in single nanocavity will offer opportunities for multifunctional devices, paving the way to integrated multi-parameter sensors, filters, nonlinear devices, and compact light sources.

© 2019 Optical Society of America under the terms of the [OSA Open Access Publishing Agreement](#)

1. Introduction

In the past two decades, photonic band gap (PBG) materials have drawn considerable attentions, due to their abilities to confine light within a volume of the order of $(\lambda/2n)^3$ in certain directions with specified frequencies [1–3]. Among all kinds of PBG structures, photonic crystal nanobeam waveguide (PCNW) is the simplest structure to be fabricated, which has only a one-dimensionally periodic pattern along the direction of propagation. By simply introducing a defect into the PCNW, the first photonic crystal nanobeam cavity (PCNC) was demonstrated in 1997 [2]. However, the quality (Q) factor of the defect mode placed within the PBG is relatively low (~ 250) due to strong scattering of light at the interfaces with abrupt changes of the refractive index. In order to suppress the light scattering and increase the Q -factor, filling factors of holes in photonic crystal reflectors are usually designed to change gradually [4–9]. Among all these studies, the deterministically design method based on mathematical descriptions proposed by Quan. et al. is the most popular, which has a clear recipe to confine the resonant modes near the PBG edges with high Q -factor and low V [8]. It is convenient to refer to the modes with resonant frequencies close to the band above and below a PBG as air modes and dielectric modes respectively based on where the energy of their modes is concentrated [1]. The unique distinct field distribution of two modes have found various applications in many research areas. For example, air modes are largely exposed to air and thus more sensitive to the change of environment, which is attractive for bio-medical sensing [10–12]. On the other hand, dielectric modes feature strong confinement in waveguide, which are adequate for integrated light sources and nonlinear process [13–17].

In addition to high Q -factor and low V , it has long been desired to achieve multiple resonances in integrated devices for the applications such as multiple parameters sensing [18–20], multiple narrow-band light sources [21], integrated nonlinear devices [22] and multifunctional devices [23,24]. While all these applications can be realized simply by combining both air and dielectric modes in single nanocavity. For the SOI-based structure, taking the simultaneous detection of temperature and liquid concentration for example, the mode with field optima at silicon region is more sensitive to the temperature change due to its large thermos-optic coefficient, while larger confinement factor in air holes is more sensitive to the concentration change due to the strong light-matter interaction. However, the study of previously reported PCNCs almost was limited only to single resonance operation, either dielectric mode or air mode [3–17]. Though by increasing the cavity length, higher order air or dielectric modes can be achieved, essentially they belong to the same kind of modes, which limits the applications [8]. Traditional multimode cavities usually are realized by cascaded PCNCs [19] or orthogonal intersecting PCNCs [25] with different resonant wavelength, which is naturally large in footprint and complex in device. Besides, multiple modes can also be enabled by using different polarization, but this will also make the device complex and the frequency of the resonant modes could not be adjusted independently [26,27]. Hence, it is necessary to simultaneously confine multiple resonances with different field distributions in a single cavity to make accurate detection.

Therefore, here we propose and demonstrate a design method to confine both air and dielectric modes in a single nanocavity in mid-infrared (MIR). Note that the design principle can also be applied in the near-infrared wavelength range. For sensing, MIR is an important wavelength range since it contains the fingerprints of many chemicals and biological agents. Basically, the coexistence of two modes is enabled by carefully tapering the geometry to make the bands move into opposite directions to confine both air and dielectric bands simultaneously. Besides, compared with the traveling wave regime, the group index of PCNW near the PBG edges can be engineered to be very large, leading to a significant decrease in the group velocity of light, which is a powerful new route for enhanced optical trapping and guiding [28,29]. Hence, central periodic mirrors are designed to reduce the tapered section induced perturbation and to make the resonance modes move from traveling wave regime to slow light regime. High experimental Q -factors of 2.32×10^4 and 1.59×10^4 are achieved at the resonance wavelength of about $3.875\mu\text{m}$ and $3.728\mu\text{m}$ for fundamental dielectric and air modes respectively. And the footprint of the cavity is only $\sim 36 \times 1.3\mu\text{m}^2$ (length \times width). In addition, the responses of air and dielectric modes in single PCNC to the changes of external refractive index and temperature are discussed, showing the potential of the proposed structure for multi-parameter sensing.

Moreover, on one hand, for sensing using molecular absorption fingerprints [30–32], there is an increasing need to manipulate multiple resonances over wider spectra ranges to access more chemical information [33]. On the other hand, for some nonlinear optical interactions such as frequency conversion, it is desirable to have good spatial field overlap between different resonant modes [34]. Therefore, to take one step further to extend to the application of the proposed device for broadband operation and non-linear applications without the sacrifice of footprint, aperiodic structures have attracted our attention, which can achieve dual-PBG by mixing of two periodic structures with different periodicities [35–37]. Enlightened by our interpretation with periodic central mirrors, we further introduce deterministic aperiodic central mirrors and experimentally demonstrate the coexistence of multiple sets of air and dielectric modes. Our work offers opportunities to multifunctional and multi-wavelength nanocavities, paving the way to integrated light source, filtering, biomedical sensing and environmental monitoring.

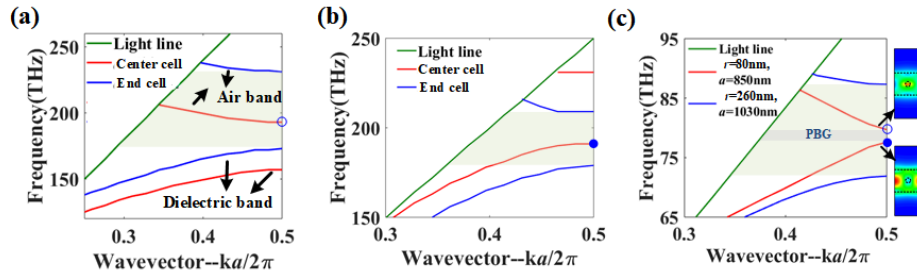


Fig. 1. Calculated TE band diagrams of the PCNC for (a) previously reported air mode, (b) dielectric mode design principle and (c) our designed dual-mode design principles, respectively. The blue hollow and solid circle dots mean the confined air modes and dielectric modes, respectively.

2. Design principle

Existence of air and dielectric modes are closely related to the photonic diagram of photonic crystal reflectors, thus it is critical to taper the holes properly. For previously design principle of the reflectors, both air and dielectric bands shift in the same direction as the mirror strength increases from center to both sides by changing the filling factors, as shown in Figs. 1(a) and 1(b). Therefore, only air or dielectric modes can be confined in a single cavity. Here, we change the period and radius of holes array simultaneously to make the air and dielectric bands move in opposite directions in the tapering section to confine both air and dielectric bands simultaneously, as shown in Fig. 1(c). From the graph, we can see that the bandgaps of inner and outer holes are well aligned, and thus we can expect coexistence of air and dielectric modes in single nanocavity. Details of the design are as follows.

Figure 2(a) shows the schematic of our proposed PCNC supporting both air and dielectric modes, which consists of an array of circular air holes etched into a silicon strip waveguide. The taper sections are treated as reflectors to confine both air and dielectric modes. The central mirror sections are designed to make the air and dielectric modes move deeper into the band edges. In Fig. 2(a), r_I , r_{Ntaper} , a_I and a_{Ntaper} indicate the radius and lattice constant of the inner and outer holes in the taper sections, respectively. For the inner periodic mirror section, the radius r_m and lattice constant a_m are kept the same as r_I and a_I , respectively.

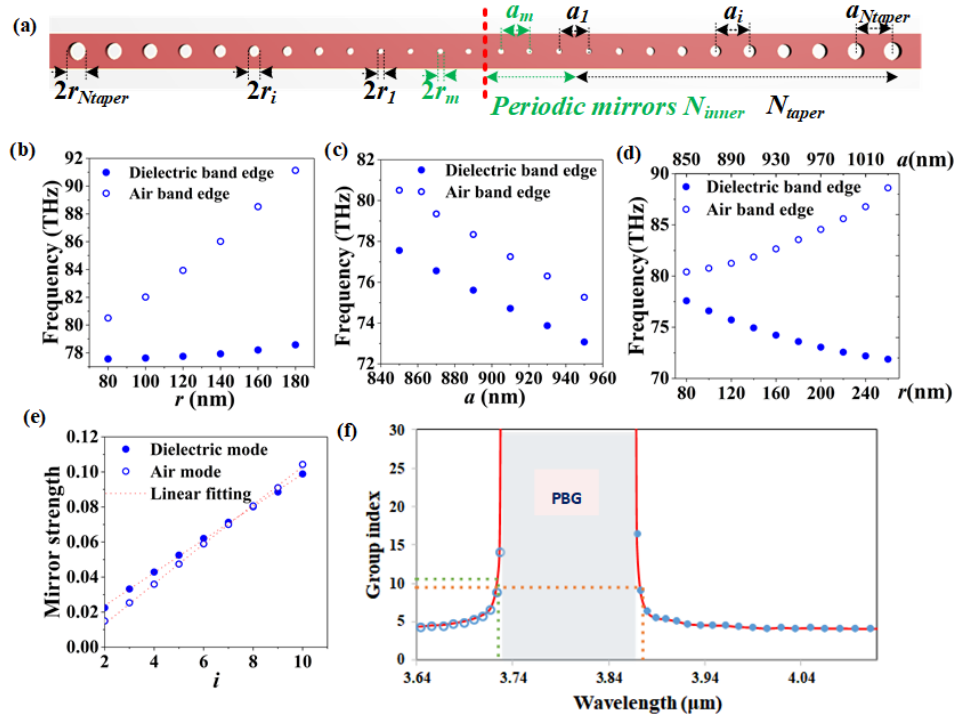


Fig. 2. (a) Schematics of the proposed structure. The structure is symmetric with respect to its center (red dashed line). For the taper section, both lattice constant and radius are linearly modulated from the center to both sides. For the inner section, the lattice constant and radius are kept as constant as a_i and r_i respectively. (b) Change of dielectric and air band edge frequencies versus radius r . The waveguide width and lattice constant are kept as $1.30\mu\text{m}$ and 850nm respectively. (c) Change of dielectric and air band edge frequencies versus lattice constant a . The waveguide width and radius are kept as $1.30\mu\text{m}$ and 80nm respectively. (d) Change of dielectric and air band edge frequencies versus lattice constant and hole radius with a step of 20nm simultaneously. (e) The mirror strength as a function of taper numbers after linear tapering. (f) Correspondingly derived group index constant from the air and dielectric bands of the central cell.

The thickness of the nanobeam is 500nm , determined by the thickness of the device layer of our SOI wafer. For mid-IR SOI device, the material absorption loss should not be neglected, which mainly comes from the electrical field overlap in the buried oxide. To minimize the loss and ensure single mode here, the waveguide width w is chosen as $1.30\mu\text{m}$, which has an effective refractive index (n_{eff}) of ~ 2.28 at the wavelength of $3.85\mu\text{m}$ calculated by MODE Solutions. Therefore, the central lattice constant a_i is set as 850nm estimated by $a = \lambda/2n_{\text{eff}}$ to make the dielectric band edge localize at the wavelength of $\sim 3.85\mu\text{m}$. To make sure the air and dielectric band edges fit within the allowed measurement transmission spectra window for our characterization setup ($3.640\mu\text{m}$ – $4.120\mu\text{m}$) experimentally, r_i is set as 80nm such that the PBG ranging from 77.59THz to 80.5THz ($3.726\mu\text{m}$ – $3.866\mu\text{m}$), as shown in Fig. 1(c).

In order to evaluate the influence of the radius (r) and lattice period (a) on the frequencies of air and dielectric band edges respectively, we simulate the band structure of unit cells when r or a is changed. As shown in Fig. 2(b), with the increase of r , the frequencies of dielectric band edges almost keep unchanged, while the air band edges are pushed to higher frequency, resulting in the increase of PBG. With the increase of a , the dielectric band edge and the air band edge are decreased synchronously, and the width of the PBG almost remains unchanged, as shown in Fig. 2(c). Therefore, by changing a and r simultaneously and properly, the air and

dielectric bands can move into opposite directions, realizing the confinement of both air and dielectric bands, as shown in Fig. 2(d). In [8], in order to reduce radiation loss, Quan. et al. make the mirror strength change linearly from the center to both sides to create a Gaussian mirror. The mirror strength γ for air and dielectric modes with different radius and lattice constant is calculated by $\sqrt{(w_2 - w_1)^2 / (w_2 + w_1)^2 - (w_{res} - w_m)^2 / w_m^2}$, where w_{res} is the proposed target resonance, w_2 , w_1 , and w_m are the air band edge, dielectric band edge, and midgap frequency of each segment, respectively. For air and dielectric modes, the target resonance frequency means the air and dielectric band edge frequency of the central cell respectively. It can be seen in Fig. 2(e) that linearly increased mirror strengths for air and dielectric modes are achieved by linear tapering a and r simultaneously with a step of 20nm from center to both sides ($a_i = a_l + 20(i-1)$, $r_i = r_l + 20(i-1)$, i increases from 1 to N_{taper}). When air and dielectric band edges move in opposite directions with approximately equal rate, similar mirror confinement for air and dielectric modes can be achieved, resulting in roughly equal Q-factors. The larger the number of taper holes is, the higher the mirror strength can be achieved, resulting in higher Q-factor. Note that the minimum variation step of 20nm is chosen by considering the experimental beam condition of Electron beam lithography.

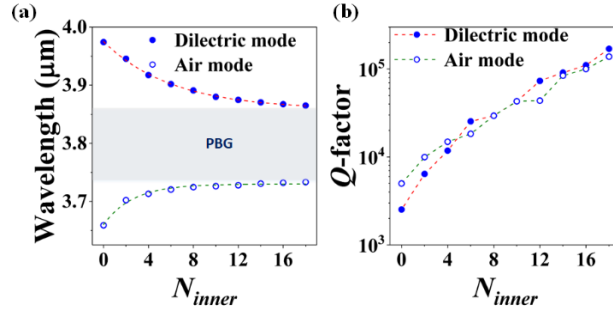


Fig. 3. Simulated (a) resonance wavelength λ and (b) Q-factor of the fundamental air and dielectric resonant modes as a function of the number of central mirrors N_{inner} . N_{taper} is set as 10.

The group index extracted from the band diagram of the central cell in Fig. 1(c) using $n_g = c/v_g = c/(dw/dk)$ are plotted in Fig. 2(f). As shown, the group index (n_g) is ~ 4 in the spectral regions away from the PBG edges. And it can be engineered to be very large near the PBG edges, leading to a significant decrease in the group velocity of light, which is attractive for enhanced optical trapping and guiding. Usually, the perturbation induced by the taper section will make the resonances modes have a shift of about 2% compared with target resonant wavelengths at PBG edges, resulting in the resonance modes lying in traveling wave regime. Therefore, central mirrors are designed here to make the air and dielectric modes move deeper into the band edges to achieve slow light-enhanced effect. In this way, the structure can be treated as a Fabry-Perot cavity, therefore, we can derive the resonance equation in PCNC cavities as below:

$$8\pi k_0 N_{inner} a_1 + 2\varphi_r = 2m\pi, \quad (1)$$

where φ_r is the reflection response from taper section, m is the mode order, k_0 is the wave vector. For dielectric and air bands, the frequency $w(k)$, which is a function of wave vector k , using the Taylor expansion at $ka_l/2\pi = 0.5$, can be written as:

$$\omega(k) \approx \omega_0 + \frac{c}{2} \frac{d(1/n_g)}{dk} \left(k - \frac{\pi}{a_1}\right)^2, \quad (2)$$

where ω_0 is the frequency of dielectric or air band edges, and n_g is the group index. The first degree is neglected because the group velocity at band edges usually tends to be zero. The second order coefficient is related with the group velocity dispersion. Based on the equations above, we can derive the resonance frequency of the fundamental air mode and dielectric mode as ($k_0 = k\pi/a$):

$$\omega - \omega_0 \approx \frac{c}{2} \frac{d(1/n_g)}{dk} \left(\frac{\phi_r}{4a_1} \right)^2 \frac{1}{N_{inner}^2}. \quad (3)$$

We can see that ω will be closer to the bandgap edges with an inverse square relation with the increase of N_{inner} . The simulated results shown in Fig. 3(a) confirm our interpretation. Here, N_{taper} is set as 10. As shown, with the increase of the number of mirror holes N_{inner} , the resonant modes move deeper into the band edges but saturate as the resonant wavelength approaches the PBG edges which unequivocally confirms the PBG effect. In this way, when N_{inner} is larger than 10, n_g of the fundamental resonant modes can be enhanced at least for two-folds compared with the structure without central mirrors, as shown in Fig. 1(f). In addition, Q values of fundamental modes increase with the increase of N_{inner} , which can be attributed to the higher mirror reflectance, and smaller scattering loss. High Q -factors above 10^5 can be obtained when N_{inner} is large enough, as shown in Fig. 3(b).

3. Results and analysis

3.1. Device fabrication and measurements

Our devices were fabricated from SOI wafers with a 500nm thick Si device layer and 2 μ m thick buried oxide. Electron beam lithography (JEOL JBX-6300-100kV) was performed using ZEP 520A resist spun at 6000rpm (\sim 300nm thick). In order to save the writing time and cost, the beam current we choose is 5nA, which has a beam diameter of \sim 15nm. An exposure dose of 300 μ C/cm² was used. The resist is developed with n-Amyl acetate developer and rinsed with IPA/MIBK. Reactive ion etching of the exposed Si regions was performed with C₄F₈, SF₆ and Ar process gases.

Figure 4(a) is the optical microscope image of the fabricated structure, in which light is coupled into the bus waveguide by the TE subwavelength grating (SWG) coupler, then passes through the PCNC, and finally gets directed out by the other grating coupler. Figure 3(b) and Fig. 3(c) are the scanning electron microscopy (SEM) images (top image, xy plane) of the fabricated nanobeam cavity section and SWG coupler section, respectively. According to the optimized design in simulation, the SWG periods are chosen as 1.9 μ m and 1.0 μ m along and perpendicular to the waveguide propagation direction, and the corresponding trench widths are 1.026 μ m and 0.260 μ m respectively, as shown in the inset of Fig. 3(c). The measured efficiency of the fabricated grating coupler is around -8 dB with 3dB bandwidth around 175nm. The measured propagation loss of the fabricated straight waveguide gradually increases from \sim 1.2 dB/cm at 3.64 μ m to \sim 12 dB/cm at 4.0 μ m. The measurements were performed using a linearly polarized continuous wave tunable MIR laser (3.64-4.12 μ m) and detector. Details of the experimental set up were discussed in our previous works [38,39].

3.2. Air and dielectric modes in single PCNC without central mirrors

The corresponding experimental transmission spectra for PCNC without central mirrors normalized to strip waveguide structure is presented in Fig. 4(d), showing good agreement with the calculated transmission spectra using three dimensional finite difference time domain (3D-FDTD) simulation method [40]. The 3D simulation domains are set as 40 μ m \times 6 μ m \times 4 μ m. A perfectly matched layer (PML) is used as boundary condition to absorb the outgoing fields, and anti-symmetrical boundary conditions along the y-directions have been exploited to save the simulation time. We use non-uniform mesh and enable it to automatically match the periodicity of the physical structure. The mesh accuracy is set as 4, and the small hole

regions are added mesh with a grid size of 5nm. The time step dt which depends on the mesh accuracy is 0.105627fs. Apparently, the transmission spectra demonstrate the realization of both fundamental air and dielectric modes in single PCNC. The corresponding calculated electric fields E for air and dielectric modes are shown in Fig. 4(e), which also reveal the presence of air and dielectric modes. It can be seen clearly that the optical field is strongly localized in air holes for the air mode, contrast to the dielectric mode which is mainly confined in silicon. An appropriate measure of the degree of concentration of the electric can be defined as $f_{air} = \int_{\epsilon=1.0} dV(\epsilon \cdot |E|^2) / \int dV(\epsilon \cdot |E|^2)$. The calculated results show that 5.06% and 3.91% of electric field energy are located in the void space for the air and dielectric modes respectively, which indicates the different electrical field distributions. It is worth noticing that the difference between the confinement factors can be improved by using larger hole sizes to increase the refractive index contrast.

The experimental fundamental air and dielectric modes exhibit Q -factor of 2924 and 4382 at the resonant wavelength of $\sim 3.655\mu\text{m}$ and $3.979\mu\text{m}$ respectively, obtained by fitting to a Lorentzian profile as shown in Fig. 4(f). The simulated Q -factors for air and dielectric modes at the resonant wavelength of $\sim 3.668\mu\text{m}$ and $\sim 3.974\mu\text{m}$ are 4021 and 2262, respectively. And the corresponding mode volume (defined as $V = \int dV \epsilon \cdot |E|^2 / (\epsilon \cdot |E|^2)_{\max}$) are $0.68(\lambda/n_{\text{si}})^3$ and $1.00(\lambda/n_{\text{si}})^3$, respectively. The fabrication induced roughness (such as imperfect circular holes, rough sidewall and lag effect) is possibly the reason for the discrepancy between the simulation and the fabrication. In addition, as shown in Fig. 4(d), compared with target resonant wavelengths at PBG edges, the resonance modes here have a wavelength shift of about 2% away from the PBG edges.

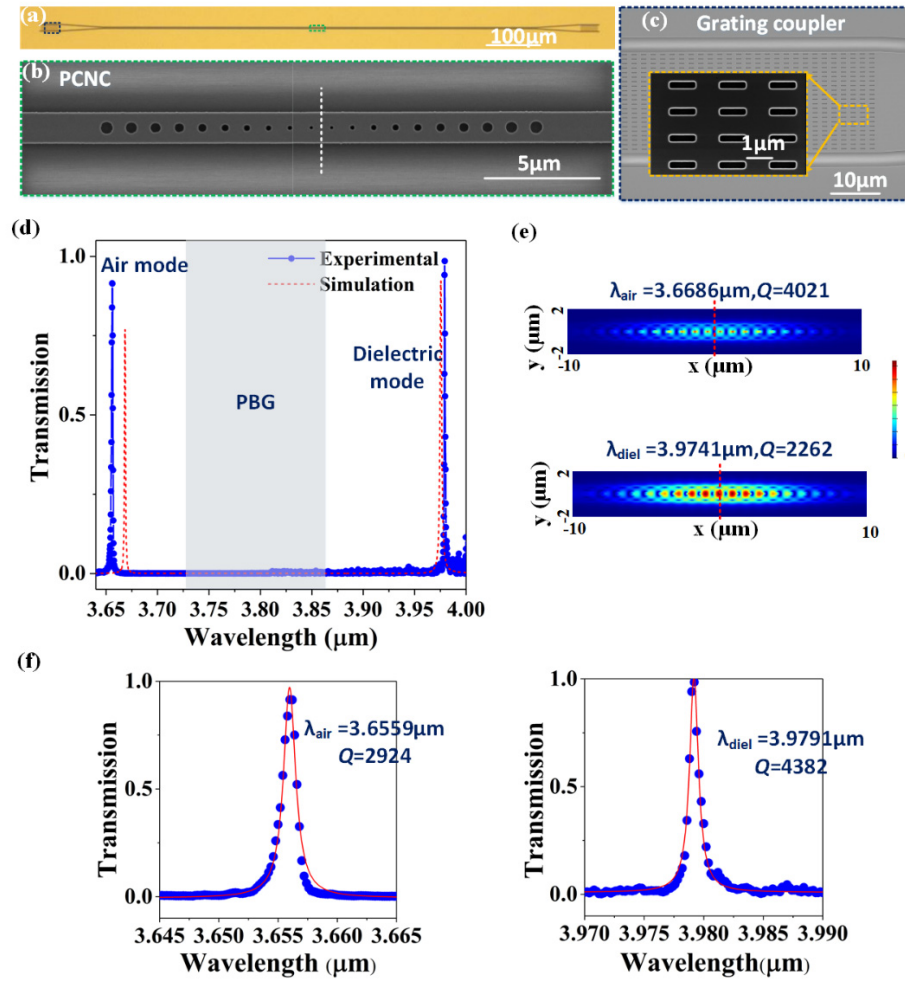


Fig. 4. (a) Optical microscope image of the fabricated device. (b) Scanning electron microscopy image of the PCNC. (c) Scanning electron microscopy images of the grating coupler. The inset shows the magnified view of the air holes. (d) Measured normalized transmission spectra and corresponding simulated transmission spectra for dual-mode PCNC with 10 tapered holes on both sides. (e) The field distributions of fundamental air mode and dielectric mode. Symmetry plane is indicated by the red dashed line. (f) Lorentzian fittings of the measured fundamental air and dielectric mode.

3.3. Air and dielectric modes in single PCNCs with central periodic mirrors

To further demonstrate the relationship between the resonance wavelength and the number of inner periodic holes N_{inner} , PCNW and a series of nanocavities with N_{inner} varying from 0 to 10 were fabricated, and the testing results are shown in Fig. 5(a). As expected, with the increase of N_{inner} , both fundamental air and dielectric modes move deeper into the band edges and have the tendency of stabilizing around the edges, which demonstrates the interpretation of Eq. (3). Lorentzian fittings of the resonance modes are performed to reveal the measured resonance wavelengths and quality factors, and the extracted results are shown in Fig. 5(b). The FSR between fundamental air and dielectric modes are tuned from $\sim 330\text{nm}$ to $\sim 150\text{nm}$ by increasing the central mirror numbers from 0 to 10. In addition, with the increase of the central cavity length, the number of higher-order resonant modes increases and the FSR between different mode orders decreases, which also reveals the slow light-enhanced effect. The highest experimental Q -factors of 2.32×10^4 and 1.59×10^4 are achieved at the resonance

wavelength of about $3.875\mu\text{m}$ and $3.728\mu\text{m}$ for fundamental dielectric and air modes when $N_{\text{inner}} = 10$, respectively. And the insertion losses for both modes are $\sim 11\text{dB}$. The corresponding calculated electric fields E are shown in the inset of Fig. 5(c). And the calculated fraction of mode energy inside the environmental medium for the air mode is 3.97%, whereas for the dielectric mode it is 2.67%. Compared with the values of the cavity without central mirrors (5.06% and 3.91%), the results indicate that the modes moving into the slow-light regions become more confined and less sensitive to environmental changes.

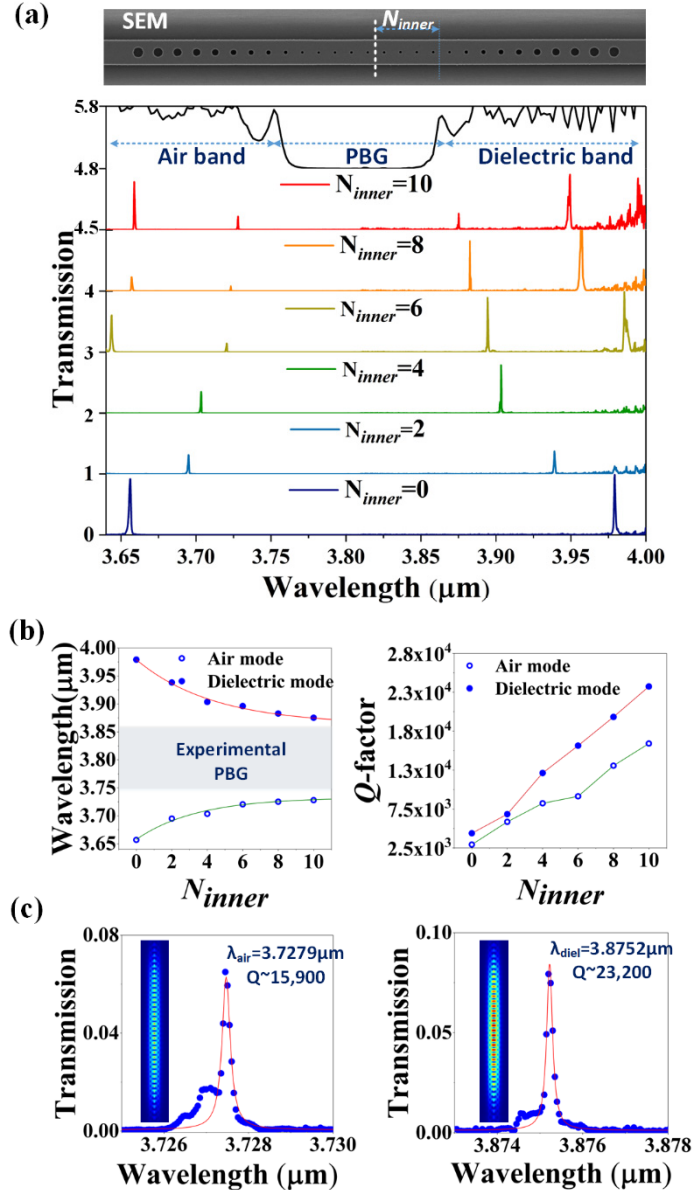


Fig. 5. (a) Measured normalized transmission spectra for PCNW and PCNCs with different number of inner mirrors from 0 to 10, and taper holes are kept constant as 10. The inset shows the SEM image of the cavity. (b) Extracted measured λ and Q-factor of the fundamental air and dielectric resonant modes as a function of the number of N_{inner} . (c) Lorentzian fittings of the measured fundamental air and dielectric mode.

Therefore, in this section, we demonstrated the deterministic design method to confine both air and dielectric modes simultaneously with determined resonance wavelengths and high Q -factors. Compared with previously demonstrated Mid-infrared SOI resonators [41–43], our device has exhibited higher Q -factor and smaller footprint.

3.4. Sensing characterizes of air and dielectric modes

Here, we discuss the response of the air and dielectric modes in single PCNC to external environment change in theoretical and simulation. Based on the perturbation theory [1], the frequency shift $\Delta\omega$ caused by a small perturbation can be expressed as

$$\Delta\omega/\omega \approx -(\Delta n/n) \cdot (\text{fraction of } \int \epsilon |E|^2 \text{ in the perturbed regions}), \quad (4)$$

where Δn is the refractive index change amount of the material caused by perturbations.

If we make the application as air or liquid sensing, the perturbed regions mean the air regions. Therefore, for both resonance modes, the wavelength shifts caused by refractive index change can be expressed as

$$\Delta\omega/\omega \approx -\Delta\lambda/\lambda \approx -(\Delta n_{\text{air}}/n_{\text{air}}) \cdot f_{\text{air}}, \quad (5)$$

deriving the refractive index sensitivity (S_n) expression of

$$S_n = \Delta\lambda/\Delta n \approx \lambda \cdot f_{\text{air}}. \quad (6)$$

Therefore, the theoretical sensitivity for fundamental air mode for the structure with 10 inner holes and 10 taper holes is 160nm/RIU, and the sensitivity of the fundamental dielectric mode is 105 nm/RIU, 55 nm/RIU lower than that of the air band mode. The sensitivities are in good agreement with the value of 186nm/RIU and 135nm/RIU fitted from 3D-FDTD simulations as shown in Fig. 6(a), where the resonance wavelength is calculated with varying the environment refractive index.

While for temperature sensing in air environment, the perturbed regions mean the silicon region [19]. Ignoring dimension changes induced by thermal expansion, the wavelength shifts caused by temperature change can be expressed as

$$\Delta\omega/\omega \approx -\Delta\lambda/\lambda \approx -(\Delta n_{\text{si}}/n_{\text{si}}) \cdot f_{\text{si}} = -(\Delta n_{\text{si}}/\Delta T) \cdot (\Delta T/n_{\text{si}}) \cdot f_{\text{si}}, \quad (7)$$

deriving the temperature sensitivity (S_T) expression of

$$S_T = \Delta\lambda/\Delta T \approx \lambda \cdot (\Delta n_{\text{si}}/\Delta T)/(n_{\text{si}}) \cdot f_{\text{si}}. \quad (8)$$

For the PCNC with 10 inner holes and 10 taper holes, the calculated fractions of mode energy inside the silicon for the air mode and dielectric mode are 92.16% and 94.22%, respectively. And the thermos-optic coefficient for silicon is about 1.8×10^{-4} RIU/°C. Therefore, the theoretical temperature sensitivities for air and dielectric mode are ~180pm/°C and 192pm/°C, respectively, which are in the same trend with the value of 147pm/°C and 158pm/°C fitted from 3D-FDTD simulations as shown in Fig. 6(b).

The theoretical and simulation results apparently show that the sensitivities of air and dielectric modes to external environment changes are different, showing the potential for multi-parameter sensing in single nanocavity.

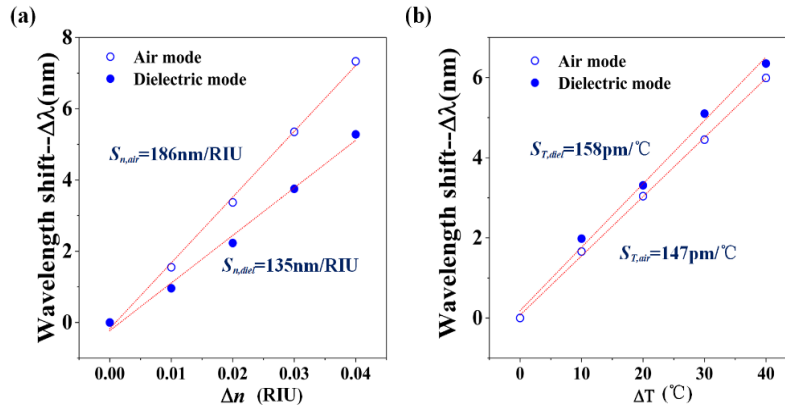


Fig. 6. The linear fitting plot of the simulated resonance shifts with the change of environmental (a) refractive index and (b) temperature.

4. Discussion

Since we have known that air modes and dielectric modes originate from rich wave vector region near bandgap edges, we can intentionally introduce more bandgaps to create multiple sets of modes, which is necessary for the broadband operation and nonlinear applications. Based on our previous work, multiple bandgaps can be achieved by using aperiodic PCNW without the sacrifice of footprint [37]. Therefore, here we design a PCNC with dual periodic central mirrors, which are created by mixing of two periodic structures with different periodicities, as shown in Fig. 7(a). The aperiodic central mirrors are formed by holes with lattice constant of 850nm and 930nm respectively. For aperiodic PCNW, N_{inner} is set as 18. For PCNC, in order to achieve higher transmission, N_{inner} and N_{taper} are set as 10 and 8 respectively. Other parameters are all consistent with the parameters of the cavity shown in Fig. 2(a). Figure 7(b) shows the simulation results of aperiodic PCNW and PCNC. In the spectra, we can obviously observe the existence of two bandgaps, and there are resonance peaks around each of them. The modes of these resonances are revealed by simulation of electric field distribution, as shown in Fig. 7(c). The field distributions reveal that modes A and C are air modes, while modes B and D are dielectric modes, which indicates the realization of multi-air and dielectric modes. The SEM images of the fabricated aperiodic PCNW and PCNC are shown in Fig. 7(d). Figure 7(e) shows the measured experimentally optical transmission, which corresponds well with the simulation results. Air and dielectric modes in the central passband are achieved at wavelength of 3.834 μm and 3.879 μm with experimentally Q -factors of 2927 and 3078, respectively. Certainly, the number of modes among the pass band and the FSR between them can be adjusted by changing N_{inner} or modifying a_1 or a_2 independently. Note that the performance of the modes can be improved by more detailed designs about the taper section.

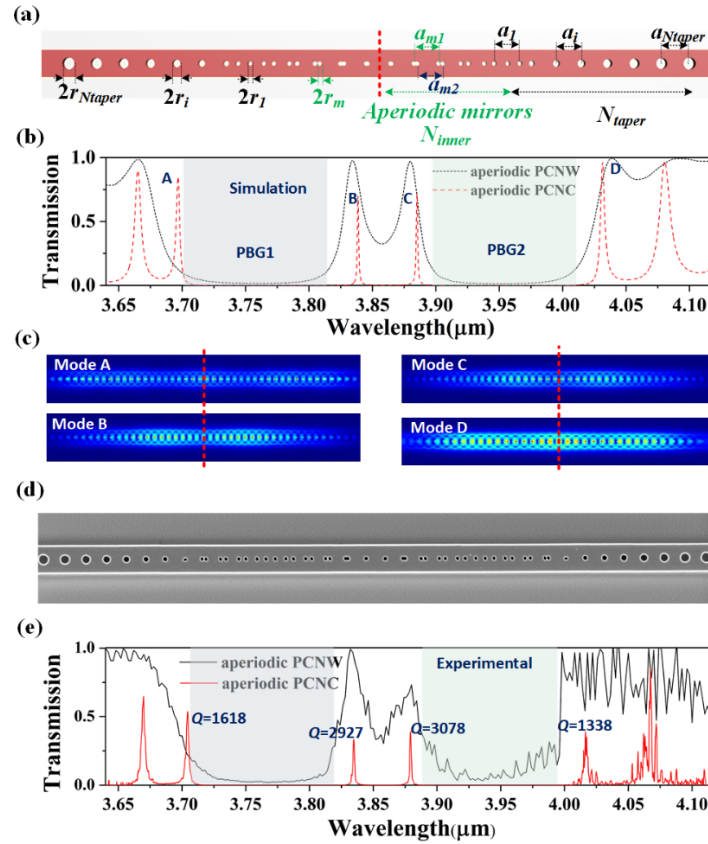


Fig. 7. (a) Schematics of the PCNC structure with aperiodic inner section. (b) Simulated transmission spectra for PCNW with 18 aperiodic inner holes and PCNC with 10 inner holes and 8 taper holes on both sides by using 3D-FDTD simulations. (c) Correspondingly field distributions of mode A, B, C and D. (d) SEM image of the fabricated cavity. (e) Correspondingly measured normalized transmission spectra and fitted Q -factors.

5. Conclusion

In conclusion, we reported the development of single PCNC supporting both air and dielectric modes. Firstly, we carefully engineer the taper profile of the PCNC so that both air and dielectric bands can be confined. Secondly, we study the design of multimode nanocavities by interpreting the air modes and dielectric modes as slow light resonance in cavities by introducing central periodic mirrors. Experimentally high Q -factors of 1.90×10^4 and 2.56×10^4 at resonance wavelengths of $3.728\mu\text{m}$ and $3.875\mu\text{m}$ for air and dielectric modes are achieved respectively when the number of taper and mirror holes are both 10. The n_g of the fundamental resonant modes can be enhanced at least for two-folds compared with the structure without central mirrors. In addition, the responses of air and dielectric resonance modes to the changes of external environment are discussed, showing the potential for multi-parameter sensing in single PCNC. Thirdly, in order to extend to the application of the proposed device for broadband operation and non-linear applications without the sacrifice of footprint, we further introduce aperiodic mirrors into nanocavities, which can support multiple sets of air modes and dielectric modes. We envision that the concepts in optical mode engineering will extend to the design of multiwavelength and multifunctional nanocavities with high performances, paving the way to photonic integrated circuit and compact sensors.

Funding

NRF-CRP15-2015-02 “Piezoelectric Photonics Using CMOS Compatible AlN Technology for Enabling the Next Generation Photonics ICs and Nanosensors” (WBS: R-263-000-C24-281) at National University of Singapore; “Hybrid Integration of Flexible Power Source and Pressure Sensors” (R-263-501-012-133) at National University of Singapore; National Natural Science Foundation of China (61372038 and 61431003); P. R. China, Fund of Joint Laboratory for Undersea Optical Networks; China Scholarship Council (201706470024); NRF-ISF “Reconfigurable data center optical interconnects using fast nanophotonic MEMS waveguide switches” (WBS: R-263-000-C64-281) at National University of Singapore.

Acknowledgments

Sun Fujun thanks the China Scholarship Council for supporting this work (File No. 201706470024). The authors thank for Wang Zheng for help with checking the manuscript.

Disclosures

The authors declare that there are no conflicts of interest related to this article.

References

1. J. D. Joannopoulos, S. G. Johnson, J. N. Winn, and R. D. Meade, *Photonic Crystals: Molding the Flow of Light* (Princeton University, 2011).
2. J. S. Foresi, P. R. Villeneuve, J. Ferrera, E. R. Thoen, G. Steinmeyer, S. Fan, J. D. Joannopoulos, L. C. Kimerling, H. I. Smith, and E. P. Ippen, “Photonic-bandgap microcavities in optical waveguides,” *Nature* **390**(6656), 143–145 (1997).
3. O. Painter, R. K. Lee, A. Scherer, A. Yariv, J. D. O’Brien, P. D. Dapkus, and I. Kim, “Two-dimensional photonic band-gap defect mode laser,” *Science* **284**(5421), 1819–1821 (1999).
4. P. Lalanne, S. Mias, and J. Hugonin, “Two physical mechanisms for boosting the quality factor to cavity volume ratio of photonic crystal microcavities,” *Opt. Express* **12**(3), 458–467 (2004).
5. M. Notomi, E. Kuramochi, and H. Taniyama, “Ultrahigh-Q nanocavity with 1D photonic gap,” *Opt. Express* **16**(15), 11095–11102 (2008).
6. A. R. M. Zain, N. P. Johnson, M. Sorel, and R. M. De La Rue, “Ultra high quality factor one dimensional photonic crystal/photonic wire micro-cavities in silicon-on-insulator (SOI),” *Opt. Express* **16**(16), 12084–12089 (2008).
7. P. B. Deotare, M. W. McCutcheon, I. W. Frank, M. Khan, and M. Lončar, “High quality factor photonic crystal nanobeam cavities,” *Appl. Phys. Lett.* **94**(12), 121106 (2009).
8. Q. Quan and M. Loncar, “Deterministic design of wavelength scale, ultra-high Q photonic crystal nanobeam cavities,” *Opt. Express* **19**(19), 18529–18542 (2011).
9. S. Hu and S. M. Weiss, “Design of photonic crystal cavities for extreme light concentration,” *ACS photon.* **3**(9), 1647–1653 (2016).
10. Y. Chen, W. S. Fegadolli, W. M. Jones, A. Scherer, and M. Li, “Ultrasensitive gas-phase chemical sensing based on functionalized photonic crystal nanobeam cavities,” *ACS Nano* **8**(1), 522–527 (2014).
11. F. Liang and Q. Quan, “Detecting single gold nanoparticles (1.8 nm) with ultrahigh-Q air-mode photonic crystal nanobeam cavities,” *ACS Photonics* **2**(12), 1692–1697 (2015).
12. S. Kim, H. M. Kim, and Y. H. Lee, “Single nanobeam optical sensor with a high Q-factor and high sensitivity,” *Opt. Lett.* **40**(22), 5351–5354 (2015).
13. Y. Zhang, M. Khan, Y. Huang, J. Ryou, P. Deotare, R. Dupuis, and M. Lončar, “Photonic crystal nanobeam lasers,” *Appl. Phys. Lett.* **97**(5), 051104 (2010).
14. N. Niu, A. Woolf, D. Wang, T. Zhu, Q. Quan, R. A. Oliver, and E. L. Hu, “Ultra-low threshold gallium nitride photonic crystal nanobeam laser,” *Appl. Phys. Lett.* **106**(23), 231104 (2015).
15. P. Lee, T. Lu, and L. Chiu, “Dielectric-band photonic crystal nanobeam lasers,” *J. Lightwave Technol.* **31**(1), 36–42 (2013).
16. R. Miura, S. Imamura, R. Ohta, A. Ishii, X. Liu, T. Shimada, S. Iwamoto, Y. Arakawa, and Y. K. Kato, “Ultralow mode-volume photonic crystal nanobeam cavities for high-efficiency coupling to individual carbon nanotube emitters,” *Nat. Commun.* **5**(1), 5580 (2014).
17. S. Kim, J. Jin, Y. J. Kim, I. Y. Park, Y. Kim, and S. W. Kim, “High-harmonic generation by resonant plasmon field enhancement,” *Nature* **453**(7196), 757–760 (2008).
18. Y. Zhang, Y. Zhao, H. Hu, “Miniature photonic crystal cavity sensor for simultaneous measurement of liquid concentration and temperature,” *Sensor Actuat. Biol. Chem.* **216**, 563–571 (2015).
19. P. Liu and Y. Shi, “Simultaneous measurement of refractive index and temperature using cascaded side-coupled photonic crystal nanobeam cavities,” *Opt. Express* **25**(23), 28398–28406 (2017).

20. J. Hromadka, S. Korposh, M. C. Partridge, S. W. James, F. Davis, D. Crump, and R. P. Tatam, "Multi-parameter measurements using optical fibre long period gratings for indoor air quality monitoring," *Sensor Actuat. Biol. Chem.* **244**, 217–225 (2017).
21. F. Pyatkov, V. Fütterling, S. Khasminskaya, B. S. Flavel, F. Hennrich, M. M. Kappes, R. Krupke, and W. H. P. Pernice, "Cavity-enhanced light emission from electrically driven carbon nanotubes," *Nat. Photonics* **10**(6), 420–427 (2016).
22. S. Buckley, M. Radulaski, J. L. Zhang, J. Petykiewicz, K. Biermann, and J. Vučković, "Multimode nanobeam cavities for nonlinear optics: high quality resonances separated by an octave," *Opt. Express* **22**(22), 26498–26509 (2014).
23. D. Sell, J. Yang, S. Doshay, R. Yang, and J. A. Fan, "Large-angle, multifunctional metagratings based on freeform multimode geometries," *Nano Lett.* **17**(6), 3752–3757 (2017).
24. D. Sell, J. Yang, S. Doshay, and J. A. Fan, "Periodic Dielectric Metasurfaces with High-Efficiency, Multiwavelength Functionalities," *Adv. Opt. Mater.* **5**(23), 1700645 (2017).
25. K. Rivoire, S. Buckley, and J. Vučković, "Multiply resonant high quality photonic crystal nanocavities," *Appl. Phys. Lett.* **99**(1), 013114 (2011).
26. Y. Zhang, M. W. McCutcheon, I. B. Burgess, and M. Loncar, "Ultra-high-Q TE/TM dual-polarized photonic crystal nanocavities," *Opt. Lett.* **34**(17), 2694–2696 (2009).
27. M. W. McCutcheon, P. B. Deotare, Y. Zhang, and M. Loncar, "High-Q transverse-electric/transverse-magnetic photonic crystal nanobeam cavities," *Appl. Phys. Lett.* **98**(11), 111117 (2011).
28. M. G. Scullion, Y. Arita, T. F. Krauss, and K. Dholakia, "Enhancement of optical forces using slow light in a photonic crystal waveguide," *Optica* **2**(9), 816–821 (2015).
29. K. Qin, S. Hu, S. T. Retterer II, I. I. Kravchenko, and S. M. Weiss, "Slow light Mach-Zehnder interferometer as label-free biosensor with scalable sensitivity," *Opt. Lett.* **41**(4), 753–756 (2016).
30. X. Zhang, G. Zhou, P. Shi, H. Du, T. Lin, J. Teng, and F. S. Chau, "On-chip integrated optofluidic complex refractive index sensing using silicon photonic crystal nanobeam cavities," *Opt. Lett.* **41**(6), 1197–1200 (2016).
31. B. Dong, T. Hu, X. Luo, Y. Chang, X. Guo, H. Wang, D. L. Kwong, G. Q. Lo, and C. Lee, "Wavelength-Flattened Directional Coupler Based Mid-Infrared Chemical Sensor Using Bragg Wavelength in Subwavelength Grating Structure," *Nanomaterials (Basel)* **8**(11), 893 (2018).
32. Y. Chen, H. Lin, J. Hu, and M. Li, "Heterogeneously integrated silicon photonics for the mid-infrared and spectroscopic sensing," *ACS Nano* **8**(7), 6955–6961 (2014).
33. D. Rodrigo, A. Tittl, A. John-Herpin, O. Limaj, and H. Altug, "Self-Similar Multiresonant Nanoantenna Arrays for Sensing from Near-to Mid-Infrared," *ACS Photonics* **5**(12), 4903–4911 (2018).
34. A. Rodríguez, M. Soljačić, J. D. Joannopoulos, and S. G. Johnson, " $\chi(2)$ and $\chi(3)$ harmonic generation at a critical power in inhomogeneous doubly resonant cavities," *Opt. Express* **15**(12), 7303–7318 (2007).
35. A. M. Vyunishchev, P. S. Pankin, S. E. Svyakhovskiy, I. V. Timofeev, and S. Y. Vetrov, "Quasiperiodic one-dimensional photonic crystals with adjustable multiple photonic bandgaps," *Opt. Lett.* **42**(18), 3602–3605 (2017).
36. Z. V. Vardeny, A. Nahata, and A. Agrawal, "Optics of photonic quasicrystals," *Nat. Photonics* **7**(3), 177–187 (2013).
37. J. Wei, F. Sun, B. Dong, Y. Ma, Y. Chang, H. Tian, and C. Lee, "Deterministic aperiodic photonic crystal nanobeam supporting adjustable multiple mode-matched resonances," *Opt. Lett.* **43**(21), 5407–5410 (2018).
38. N. Chen, B. Dong, X. Luo, H. Wang, N. Singh, G. Q. Lo, and C. Lee, "Efficient and broadband subwavelength grating coupler for 3.7 μm mid-infrared silicon photonics integration," *Opt. Express* **26**(20), 26242–26256 (2018).
39. Y. Ma, B. Dong, B. Li, J. Wei, Y. Chang, C. P. Ho, and C. Lee, "Mid-infrared slow light engineering and tuning in 1-D grating waveguide," *IEEE J. Sel. Top. Quant.* **24**(6), 1–8 (2018).
40. Lumerical, <https://www.lumerical.com/cn/>
41. M. M. Milošević, M. Nedeljkovic, T. M. Ben Masaud, E. Jaberansary, H. M. Chong, N. G. Emerson, G. T. Reed, and G. Z. Mashanovich, "Silicon waveguides and devices for the mid-infrared," *Appl. Phys. Lett.* **101**(12), 121105 (2012).
42. T. Hu, B. Dong, X. Luo, T.-Y. Liow, J. Song, C. Lee, and G.-Q. Lo, "Silicon photonic platforms for mid-infrared applications," *Photon. Res.* **5**(5), 417–430 (2017).
43. R. Shankar, R. Leijssen, I. Bulu, and M. Loncar, "Mid-infrared photonic crystal cavities in silicon," *Opt. Express* **19**(6), 5579–5586 (2011).